International Journal of Adhesion & Adhesives 102 (2020) 102665

Contents lists available at ScienceDirect

International Journal of Adhesion and Adhesives

journal homepage: http://www.elsevier.com/locate/ijadhadh

Variation of intensity of singular stress field (ISSF) along the interface outer edge of prismatic butt joint and debonding condition expressed by the ISSF

Rei Takaki [a], Nao-Aki Noda [a,*], Fei Ren [b], Yoshikazu Sano [a], Yasushi Takase [a], Tatsujiro Miyazaki [c], Yasuaki Suzuki [d], Xin Lan [e]

[a] Department of Mechanical Engineering, Kyushu Institute of Technology, 1-1 Sensui-cho, Tobata-ku, Kitakyushu-shi, Fukuoka, 804-8550, Japan
[b] School of Mechanical and Automotive Engineering, Qilu University of Technology, No.3501, Daxue Road, Changqing, Jinan, Shandong, China
[c] Department of Mechanical Engineering, University of the Ryukyus, 1 Senbaru, Nishihara-cho, Nakagami-gun, Okinawa, 903-0213, Japan
[d] Suzuki Adhesion Institute of Technology, 131 Aza-yashiki, Ukino, Chiaki-cho, Ichinomiya-shi, Aichi, 491-0806, Japan
[e] School of Energy and Power Engineering, Shandong University, Jingshi Road, 17923#, Jinan, Shandong province, China

ARTICLE INFO

Keywords:
Adhesion
Prismatic butt joint
Intensity of singular stress field (ISSF)
Fillet
Adhesive thickness

ABSTRACT

In our previous study, the adhesive strength of butt joints having three-dimensional (3D) geometries was investigated by using the intensity of singular stress field (ISSF) in two-dimensional modelling. In this paper, by considering the 3D geometry, the ISSF variation along the butt-joint interface side is discussed to explain the experimental results. The results show that the critical ISSF distributions when debonding occur are almost the same and independent of the adhesive bondline thickness. The validity of the 2D modelling is investigated experimentally for two kinds of brittle and ductile adhesives considering the location of the maximum ISSF. It is found that the adhesive strength can be expressed as a constant value of the ISSF at the center side and also at the corner of the adhesive interface.

1. Introduction

Adhesive joints are widely used in numerous industrial sectors, such as automobile, shipbuilding and aeronautics [1–8]. Compared with traditional joints, adhesive joints have several advantages of light weight, low cost and easy to process. Therefore, structural adhesive may replace traditional joints such as welding, screw, bolt, etc. However, different material properties cause singular stress at the interface end, which may lead to debonding failure in structures [9–15]. In the previous study [12], the authors examined the effect of the adhesion layer thickness on the intensity of the singular stress field (ISSF) using two-dimensional adhesion models. The results showed that ISSF decreases with decreasing the adhesive bondline thickness due to the interference at two bonded interface sides [12]. Furthermore, the ISSF when the debonding occurs ($K_{\sigma c}$) was discussed [14] for the specimens where the JIS carbon steel S35C was bonded with an epoxy brittle adhesive and ductile adhesive.

Fig. 1 reveals that the adhesive strength can be expressed as a constant value of ISSF $K_{\sigma c}$. The critical ISSF in Fig. 1 was calculated by using 2D modelling from the experimental data in Fig. 2 [12–14,16]. The ISSF method may express the average adhesive strength within 7% error for S35C/Epoxy resin A and within 12% error for S35C/Epoxy resin B independent of adhesive thickness h. The prediction accuracy is discussed in relation to the original experimental scatter in Appendix A. The results may be improved if a more thorough statistical analysis is performed on the experimental results in Fig. 1. Although 2D modelling is simple and convenient, it is known that the corner stress singularity is stronger than the side stress singularity. However, no detail study is available where the debonding occurs in comparison with the ISSF distribution along the interface sides and corners.

In this paper, therefore, the ISSF variation will be discussed for the 3D prismatic butt joint under tension. Then, the debonding condition will be examined at the interface side and at the corner considering the ISSF distribution. The validity of two-dimensional modelling in the previous studies [12–14] will be also investigated.

2. ISSF variation analysis for 3D butt joints by applying the proportional method

In this study, the ISSF variation is analyzed by applying the proportional method used in Ref. [12–14] to the Suzuki's specimens having 3D geometries [16]. As shows in Fig. 2, Suzuki [16] investigated the remote debonding stress σ_c of the brittle and ductile adhesive. Table 1

* Corresponding author.
E-mail address: noda.naoaki844@mail.kyutech.jp (N.-A. Noda).

https://doi.org/10.1016/j.ijadhadh.2020.102665
Received 25 March 2020; Accepted 25 May 2020
Available online 29 June 2020
0143-7496/© 2020 Elsevier Ltd. All rights reserved.

Nomenclature

E_j	Young's modulus ($j = 1$: Adherend, $j = 2$: Adhesive)
e_{min}	Minimum mesh size
F_σ^{REF}	Normalized ISSF for reference problem
F_σ^{Side}	Normalized ISSF
G_j	Shear modulus ($j = 1$: Adherend, $j = 2$: Adhesive)
h	Adhesive thickness
ISSF	Intensity of singular stress field
$K_{\sigma c}$	Critical ISSF
K_σ^{2D}	ISSF for 2D model
K_σ^{REF}	ISSF for reference problem
K_σ^{Side}	ISSF for 3D model at the straight
$K_{\sigma c}^{Side}$	Critical ISSF for 3D model at the straight
K_σ^{vtx}	ISSF for 3D model at the corner
r	Distance from the interface end
W	Specimen width
α, β	Dundurs' parameter
λ	Singular index at the straight side
λ_{vtx}	Singular index at the corner
σ_c	Remote debonding stress
σ_z^F	Stress obtained from FEM
σ_z^R	Real stress
σ_z^{REF}	Stress from reference problem
σ_z	Stress for 3D butt joint at the straight
σ_z^{vtx}	Stress at the corner for 3D butt joint
σ_z^∞	Remote tensile stress
ν_j	Poisson's ratio (j = 1: Adherend, $j = 2$: Adhesive)
φ	Angle from the interface end

indicates mechanical properties for the adherend and the adhesive [16]. In Appendix B, Step-by-step elementary procedures are indicated for the readers' convenience to apply the proportional method to any 3D bonded geometries.

Table 1 also indicates the singular index at the interface side λ, which can be obtained from the characteristic equation (1) [18,19] expressed by Dundurs parameter α and β. As shown in equations (2) and (3) Dundurs parameter are expressed by Poisson's ratio ν_j and the transverse elastic modulus G_j. Table 1 also indicates the singular index at the vertex λ_{vtx} in Fig. 9, whose values were recently investigated [20].

$$\left[\sin^2\left(\frac{\pi}{2}\lambda\right)-\lambda^2\right]^2\beta^2+2\lambda^2\left[\sin^2\left(\frac{\pi}{2}\lambda\right)-\lambda^2\right]^2\alpha\beta +\lambda^2\left[\lambda^2-1\right]\alpha^2+\frac{\sin^2(\lambda\pi)}{4}=0 \tag{1}$$

$$\alpha=\frac{G_1(\kappa_2+1)-G_2(\kappa_1+1)}{G_1(\kappa_2+1)+G_2(\kappa_1+1)}$$
$$\beta=\frac{G_1(\kappa_2-1)-G_2(\kappa_1-1)}{G_1(\kappa_2+1)+G_2(\kappa_1+1)} \tag{2}$$

$$\kappa_j=\begin{cases}\dfrac{3-\nu_j}{1+\nu_j} & (plane\ stress)\\ 3-4\nu_j & (plane\ strain)\end{cases}\quad (j=1,\ 2) \tag{3}$$

The analysis code uses commercially available ANSYS 16.2 and Marc/Mentat 2012. Fig. 4 shows the analysis model. Fig. 4 (a) shows the sub-model divided by fine mesh, and Fig. 4 (b) shows the main model constructed with coarse mesh. In this study, first, analysis is performed using the model in Fig. 4 (b). Then, the displacement boundary conditions of the sub-model in Fig. 4 (a) are determined. Several models are created by changing the sub-model dimension in the z-direction to confirm that the same results are obtained under different dimensions. The analytical model is composed of 8-node hexahedron elements as shown in Fig. 4. The analysis model is analyzed using 1/8 model as shown in Fig. 3 (b). Fig. 4 shows the sub-model dimensions 0.5 mm × 1.57 × 10^{-3}mm × 3.13 × 10^{-3}mm. Then, the sub-model is analyzed by applying the obtained displacement boundary conditions.

Fig. 5 shows an example of FEM stress distributions along the adhesive interface in the prismatic butt joint when $h/W = 0.1$. This is the results of Suzuki's specimens [16] where the adherent S35C is bonded by adhesive epoxy resin. As shown in Fig. 5, in the interior region of the interface $0 \le x, y < 0.45$, FEM stress is accurate since they are independent of the mesh size and satisfy $|\sigma_z - 1| < 0.002$ under the remote tensile stress $\sigma_z^\infty = 1$. However, FEM stress values are not accurate near the interface side $|x| = 0.5$ and $|y| = 0.5$ since they vary depending on the mesh size. It should be noted that the real interface stress should go to infinity along the interface side $|x| = 0.5$ and $|y| = 0.5$. The ISSF varies depending on the location of the interface side and also the adhesive thickness. Therefore, the ISSF distributions will be discussed in the next section.

Fig. 6 shows the FEM stress σ_z^F along the interface ($x = W/2$, $0 < y < W/2$) when $h/W = 0.01$. As shown in Fig. 6, the FEM stress σ_z^F varies depending on the mesh size and different from the real stress σ_z^R. Therefore, it is necessary to distinguish σ_z^R and σ_z^F. Although the real stress σ_z^R along the interface side is always infinite, the value of σ_z^F in

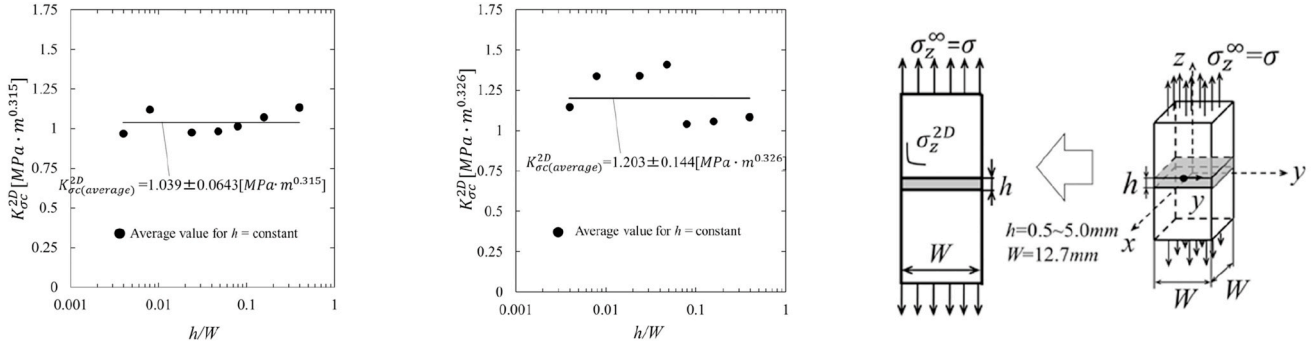

(a) For S35C/Epoxy resin A(Brittle) (b) For S35C/Epoxy resin B(Ductile) (c) 2D modelling for prismatic butt joint

Fig. 1. The adhesive strength for S35C/Epoxy resin expressed as a constant critical ISSF $K_{\sigma c}^{2D}$ from 2D modelling for two kinds of resin when $W = 12.7$ mm [14].

Fig. 6 is finite. However, from Fig. 6, the most severe singular stress σ_z^R may appear at $(x, y) = (W/2, W/2)$ since the magnitude of the finite value is largest. From Fig. 6, the FEM stress distribution at the adhesive interface edge looks almost constant in the 90% of the middle side, but it increases rapidly just after decreasing once in the range of $|x/W| \geq 0.45$ or $|y/W| \geq 0.45$. Not only at the interface corner ($|x| = W/2$, $|y| = W/2$), the real stress at the interface side is always infinite. In the following, we will focus on the ISSF instead of FEM stress by explaining a proportional method [12–15] to analyze with FEM with high accuracy.

Considering a three-dimensional adhesion model as shown in Fig. 3, the ISSF, which is represented by the symbol $K_\sigma^{Side}(y)$, is defined from the real stress by the following equation.

$$K_\sigma^{Side}(y) = \lim_{r\to 0}\left[r^{1-\lambda} \times \sigma_z^R(r, y)\right] \tag{4}$$

The dimensionless ISSF $F_\sigma^{Side}(y)$ represented by the following equation is also often used.

$$F_\sigma^{Side}(y) = \frac{K_\sigma^{Side}(y)}{\sigma_z^\infty W^{1-\lambda}} = \frac{\lim_{r\to 0}\left[r^{1-\lambda} \times \sigma_z^R(r, y)\right]}{\sigma_z^\infty W^{1-\lambda}} \tag{5}$$

Here, σ_z^∞ is a remote tensile stress in the z-direction. In equation (4), λ is a singularity index. When α (α-2β)> 0, the real stress σ_z^R becomes infinite at the interface sided having a singularity $\sigma_z^R \propto 1/r^{1-\lambda} (\lambda < 1)$ [18, 19].

Since FEM stress σ_z^F varies depending on FEM mesh size, in the previous study, FEM analysis was performed to the unknown and the reference problems by aligning the same FEM mesh patterns around the interface edge. Here, the unknown problem is the problem to be analyzed, and the reference problem is the one whose exact solution is available. The unknown and the reference problems should have the same singular stress field with different ISSF. Step-by-step elementary procedures are indicated for the readers' convenience to apply the proportional method to any 3D bonded geometries. It should be noted that the FEM stress ratio of the unknown problem and the reference problem is focused since the FEM stress ratio may cancel the error included in FEM stress. In other words, by taking the FEM stress ratio, included FEM error can be canceled and the mesh dependency disappears if the mesh alignment and material combination of the two problems are the same [12]. The ISSF of an unknown problem can be obtained by multiplying the ratio of FEM stress and the ISSF of a reference problem chosen as the exact solution previously obtained. Since the FEM stress ratio does not have to be located at the interface end, which is called zero point in Refs. [12–14] as shown in Table 2 and Table 3, the above analysis method can be called the proportional method including the zero-point method. Here, by using an adhesive plate ($h/W = 1$) as shown in Fig. 7 (b) as a reference problem, the ISSF of this model is accurately determined from the exact solution obtained by the body force method. For the reference problem (K_σ^{REF} F_σ^{REF}, $\sigma_z^{REF,F}(r)$) and the unknown problem (K_σ^{Side}, F_σ^{Side}, $\sigma_z^F(r)$), the singularity index λ and remote tensile stress σ_z^∞ in equation (6) are the same.

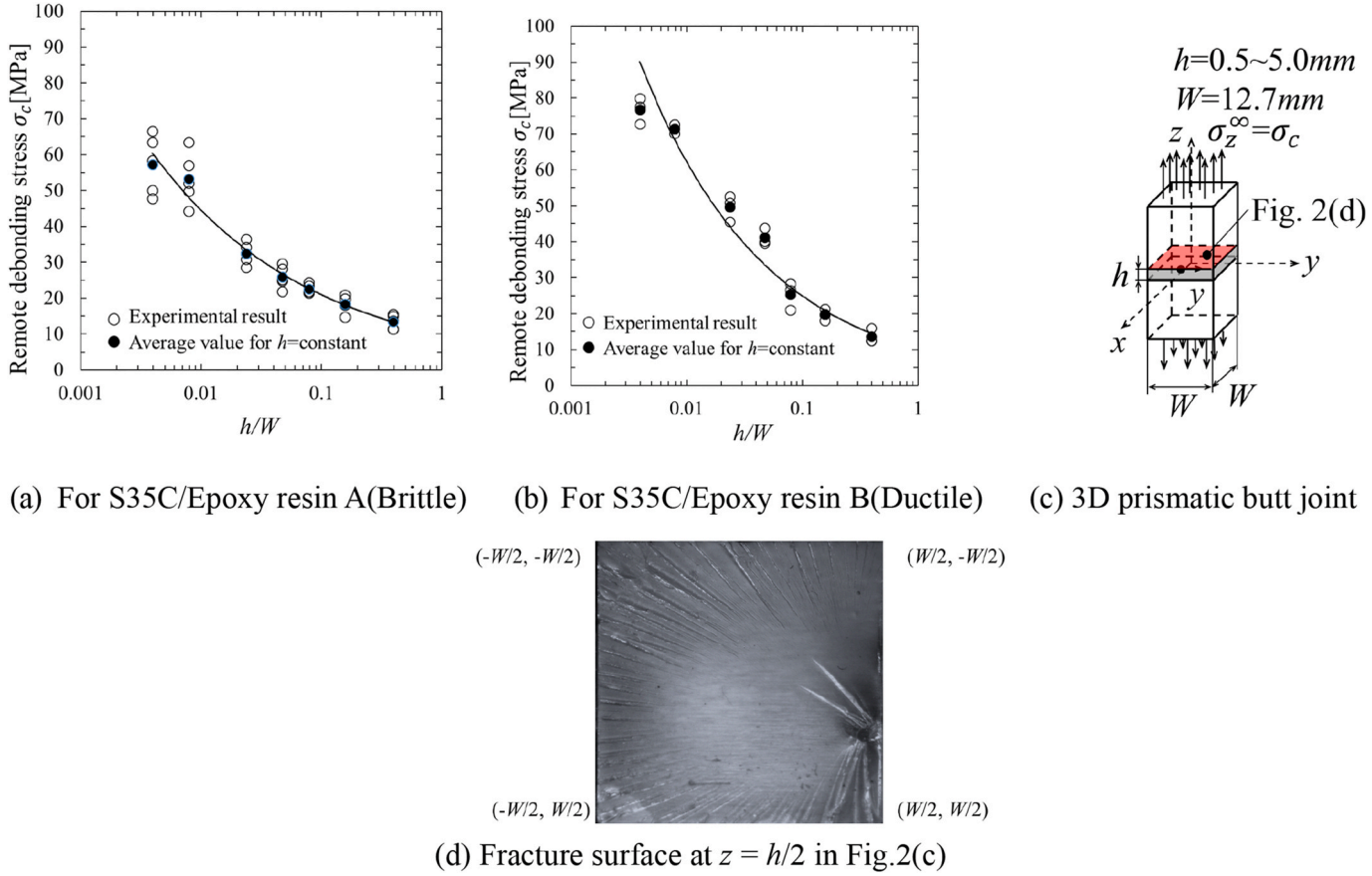

Fig. 2. Critical remote tensile stress σ_c and fracture surface for 3D butt joint with W = 12.7 mm obtained by Suzuki [16].

Table 1
Static material properties of adhesive and adherend [11].

Combination	Material		Young's modulus E [GPa]	Poisson's ratio ν	α	β	λ at side	λ at vertex
A	Adherend	S35C	210	0.30	0.969	0.199	0.685	0.608
	Adhesive	Epoxy resin A (Brittle)	3.14	0.37				
B	Adherend	S35C	210	0.30	0.978	0.188	0.674	0.596
	Adhesive	Epoxy resin B (Ductile)	2.16	0.38				

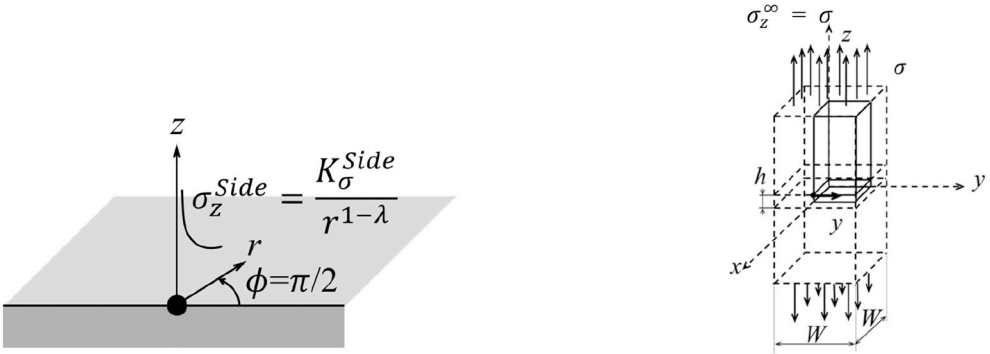

(a) Singular stress field at the straight part of interface edge (b) 1/8 model

Fig. 3. 3D butt joint geometry and singular stress field.

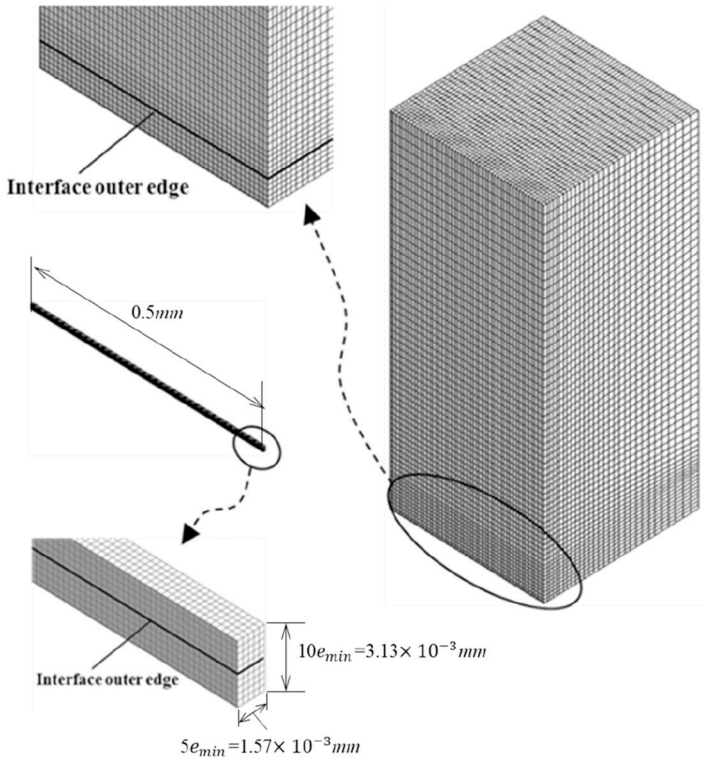

(a) Finely meshed submodel (e_{min}=3.13×10^{-4} mm) (b) Coarsely meshed model

Fig. 4. FE model for 3D butt joint.

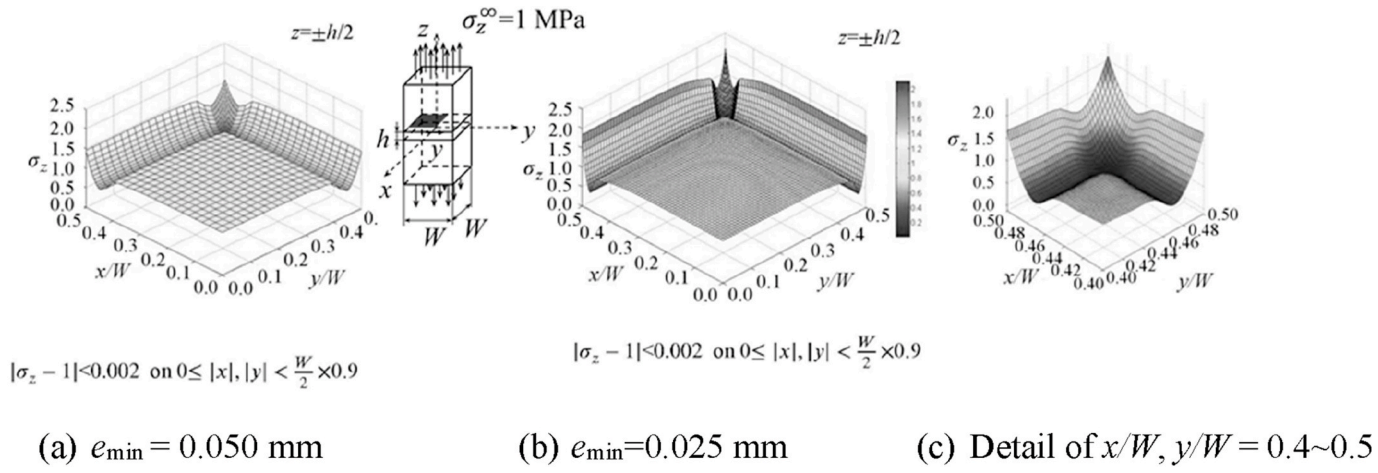

Fig. 5. FEM stress distributions $\sigma_z^{FEM}(x, y)$ along the interface $|z| = h/2$ for $h/W = 0.1$ obtained by FEM with minimum mesh size $e_{min} = 0.050$ mm and $e_{min} = 0.025$ mm.

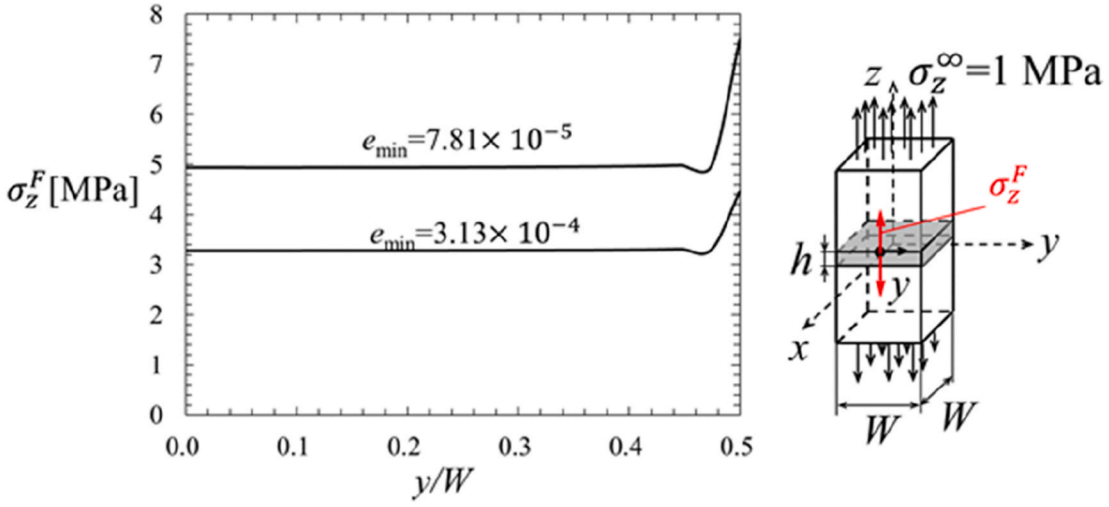

Fig. 6. Stress distributions at $x = W/2$, $0 \le y \le W/2$ ($h/W = 0.01$).

Table 2
Mesh independent analysis in Fig. 3

y/W	Smallest mesh size $e_{min} = 3.13 \times 10^{-4}$ mm around the edge			Smallest mesh size $e_{min} = 7.81 \times 10^{-5}$ mm around the edge		
	$\sigma_{z,h/W=0.01}^{Side.FEM}$	$\sigma_{z,h/W=1}^{Side.FEM}$	$\frac{\sigma_{z,h/W=0.01}^{Side.FEM}}{\sigma_{z,h/W=1}^{Side.FEM}}$	$\sigma_{z,h/W=0.01}^{Side.FEM}$	$\sigma_{z,h/W=1}^{Side.FEM}$	$\frac{\sigma_{z,h/W=0.01}^{Side.FEM}}{\sigma_{z,h/W=1}^{Side.FEM}}$
0.000	3.282	13.006	0.252	4.941	19.540	0.253
0.053	3.282	12.991	0.253	4.939	19.513	0.253
0.105	3.283	12.978	0.253	4.939	19.498	0.253
0.158	3.284	12.956	0.253	4.941	19.471	0.254
0.211	3.285	12.931	0.254	4.942	19.418	0.255
0.263	3.287	12.908	0.255	4.945	19.390	0.255
0.316	3.290	12.900	0.255	4.950	19.382	0.255
0.368	3.294	12.944	0.254	4.957	19.444	0.255
0.421	3.303	13.129	0.252	4.970	19.718	0.252
0.447	3.311	13.374	0.248	4.982	20.082	0.248
0.474	3.302	13.933	0.237	4.968	20.931	0.237
0.500	4.483	31.002	0.145	7.538	52.086	0.145

Table 3
Mesh independent ISSF ratio distribution when $K^{2D}_{\sigma,h/W=1} = 0.413$ MPa· $m^{0.315}$ with $\sigma^{\infty}_{z} = \sigma = 1$ MPa, $W = 1$ mm.

y/W	$e_{\min} = 3.13 \times 10^{-4}$ mm			$e_{\min} = 7.81 \times 10^{-5}$ mm		
	$\frac{K^{Side}_{\sigma,h/W=0.01}}{K^{Side}_{\sigma,h/W=1}}$	$\frac{K^{Side}_{\sigma,h/W=1}}{K^{2D}_{\sigma,h/W=1}}$	$K^{Side}_{\sigma,h/W=0.01}$	$\frac{K^{Side}_{\sigma,h/W=0.01}}{K^{Side}_{\sigma,h/W=1}}$	$\frac{K^{Side}_{\sigma,h/W=1}}{K^{2D}_{\sigma,h/W=1}}$	$K^{Side}_{\sigma,h/W=0.01}$
0.000	0.252	0.866	0.090	0.253	0.865	0.090
0.053	0.253	0.865	0.091	0.253	0.863	0.090
0.105	0.253	0.864	0.091	0.253	0.863	0.091
0.158	0.253	0.862	0.090	0.254	0.862	0.090
0.211	0.254	0.861	0.091	0.255	0.859	0.090
0.263	0.254	0.859	0.091	0.255	0.858	0.090
0.316	0.255	0.859	0.091	0.255	0.858	0.090
0.368	0.255	0.862	0.091	0.255	0.860	0.091
0.421	0.252	0.874	0.091	0.252	0.872	0.091
0.447	0.248	0.890	0.092	0.248	0.889	0.091
0.474	0.237	0.927	0.091	0.237	0.926	0.091
0.490	0.203	0.995	0.083	0.203	0.995	0.083
0.4994	0.147	1.211	0.074	0.147	1.211	0.074
0.4997	0.146	(1.212)	(0.073)	0.146	(1.288)	(0.078)
0.500	0.145	→∞	→∞	0.145	→∞	→∞

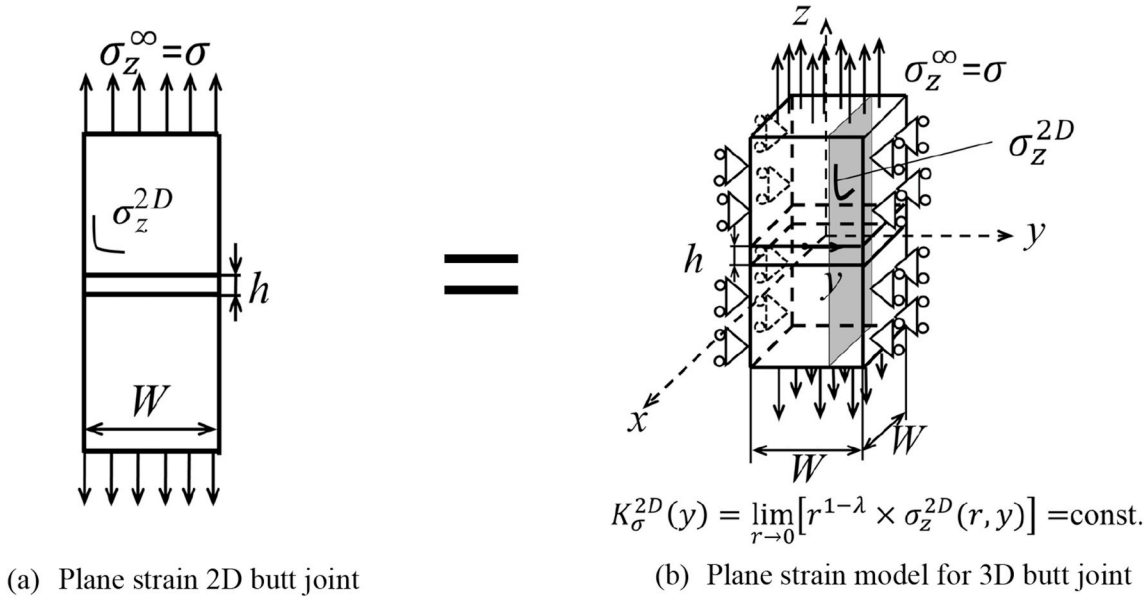

Fig. 7. Plane strain problem for 3D butt joint.

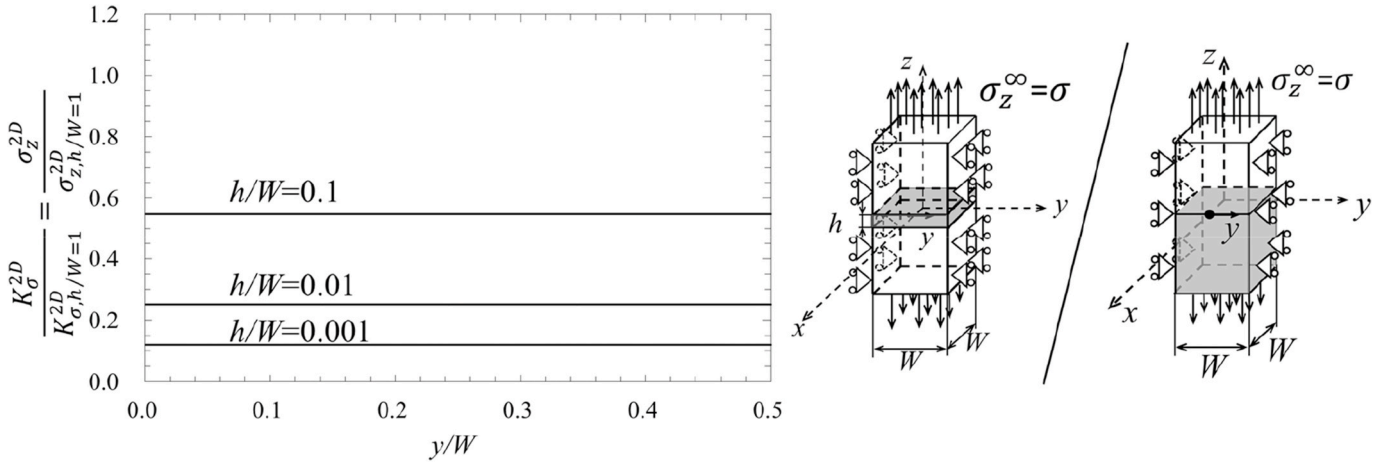

Fig. 8. ISSF ratio of $K_{\sigma}^{2D}(y)/\ K_{\sigma}^{2D}(y)|_{h/W=1}$

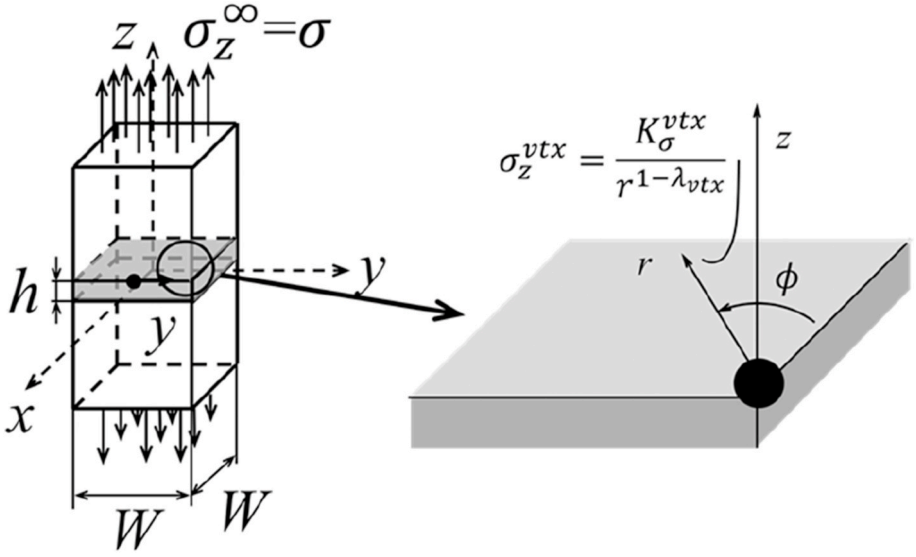

Fig. 9. Detail of corner for 3D butt joint model.

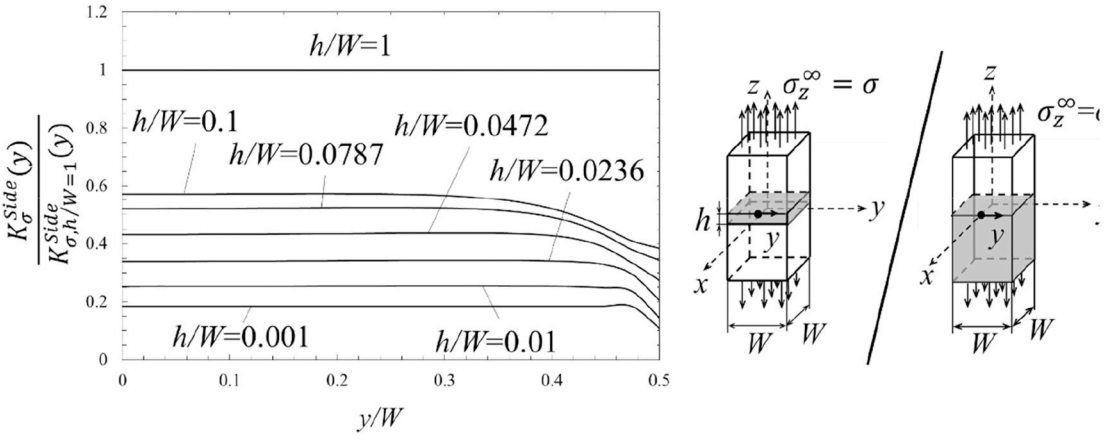

(a) For combination A

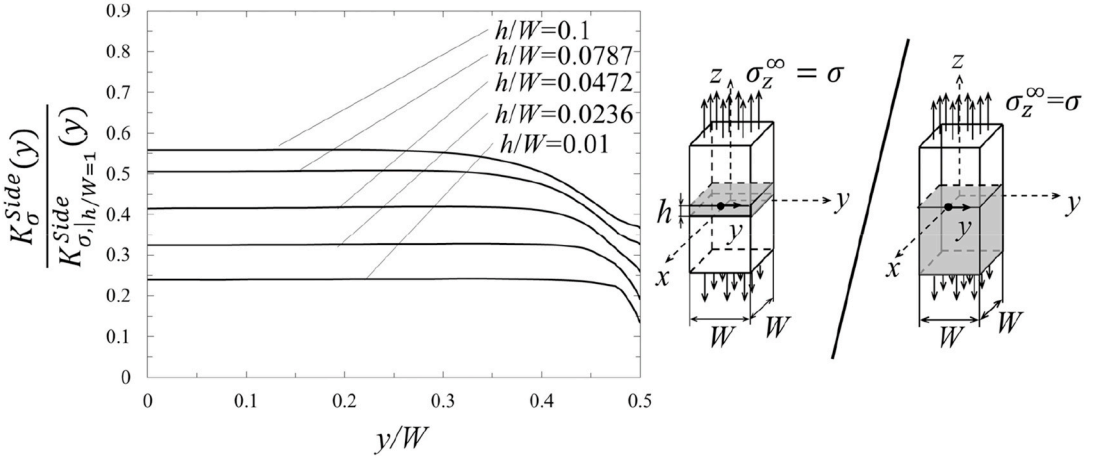

(b) For combination B

Fig. 10. ISSF ratio of $K_\sigma^{3D}(y)/K_\sigma^{3D}(y)|_{h/W=1}$

$$\frac{K_\sigma^{Side}}{K_\sigma^{REF}} = \frac{F_\sigma^{Side}\sigma_z^\infty W^{1-\lambda}}{F_\sigma^{REF}\sigma_z^\infty W^{1-\lambda}} = \frac{\lim_{r\to 0}\left[r^{1-\lambda}\times\sigma_z^R(r)\right]}{\lim_{r\to 0}\left[r^{1-\lambda}\times\sigma_z^{REF,R}(r)\right]} = \lim_{r\to 0}\frac{r^{1-\lambda}\sigma_z^R(r)}{r^{1-\lambda}\sigma_z^{REF,\ R}(r)}$$
$$= \frac{\sigma_z^F(0)}{\sigma_z^{REF,F}(0)} \quad \text{but} \quad \sigma_z^F \neq \sigma_z^R \tag{6}$$

In the previous research, using this method, we obtained the ISSF K_σ^{2D} of the 2D model in Fig. 7 (a) [12]. This 2D plane strain model corresponds to a 3D model whose displacement in one direction l is fixed as shown in Fig. 7 (b), and the results of the solution of the problems of Fig.7 (a) and Fig.7 (b) agree with each other even in FEM analysis. Therefore, in this research, the displacement in the y-direction is constrained in the 3D model, and the solution K_σ^{2D} in Fig. 7 (b) of the plane strain problem is obtained and used as the solution of the standard problem.

Table 2 shows the FEM stress along the interface side when the adhesive layer thickness $h/W = 1$ and $h/W = 0.01$. As shown in Table 2, the FEM stresses $\sigma_{z,h/W=0.01}^{Side,FEM}$, $\sigma_{z,h/W=1}^{Side,FEM}$ vary depending on the mesh size, but the FEM stress ratios $\sigma_{z,h/W=0.01}^{Side,FEM}/\sigma_{z,h/W=1}^{Side,FEM}$ are independent of the mesh size having 3-digit accuracy for any y/W.

Fig. 8 shows the ISSF in a three-dimensional model in which the displacement in the y-direction is constrained and the plane strain is used. As shown in Fig. 8, in the case of $\varepsilon_y = 0$, ISSF always shows a constant value regardless of y. The solution of plane distortion with $\varepsilon_y = 0$ in this three-dimensional model agrees with the results [12–14] of the two-dimensional model as shown in Fig. 7 (a). The result of two-dimensional adhesive bonded plate $h/W = 1$ is obtained by the body force method and can be used as the solution of the reference problem as a substantially exact solution.

In a similar way, considering a three-dimensional adhesion model as shown in Fig. 3, the ISSF denoted by $K_\sigma^{Side}(y)$ is defined from the real stress by the following equation.

$$K_\sigma^{Side}(y) = \lim_{r\to 0}\left[r^{1-\lambda}\times\sigma_z^R(r,y)\right] \tag{7}$$

The dimensionless value $F_\sigma^{Side}(y)$ defined by the following equation is also often used.

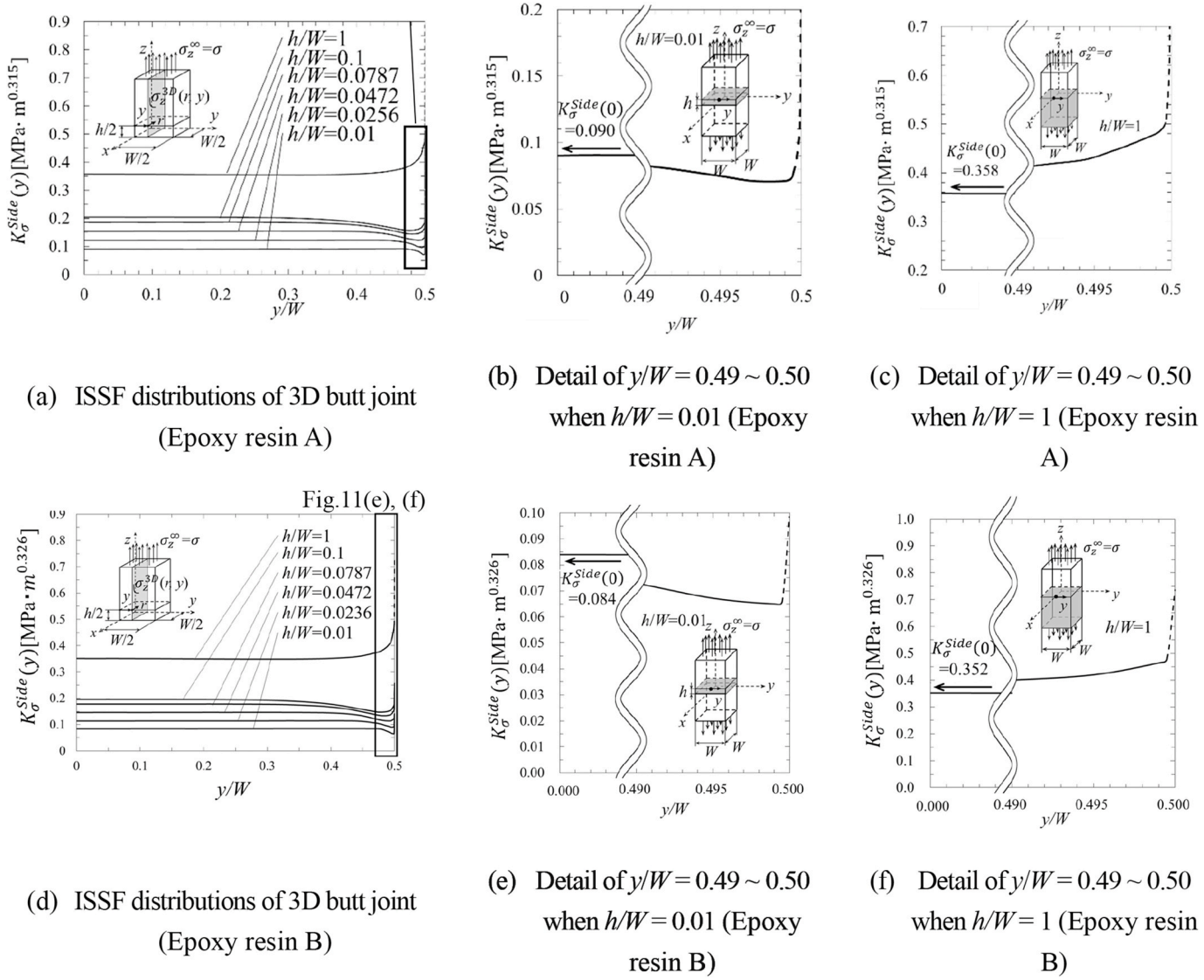

(a) ISSF distributions of 3D butt joint (Epoxy resin A)

(b) Detail of $y/W = 0.49 \sim 0.50$ when $h/W = 0.01$ (Epoxy resin A)

(c) Detail of $y/W = 0.49 \sim 0.50$ when $h/W = 1$ (Epoxy resin A)

Fig.11(e), (f)

(d) ISSF distributions of 3D butt joint (Epoxy resin B)

(e) Detail of $y/W = 0.49 \sim 0.50$ when $h/W = 0.01$ (Epoxy resin B)

(f) Detail of $y/W = 0.49 \sim 0.50$ when $h/W = 1$ (Epoxy resin B)

Fig. 11. ISSF distribution of 3D butt joint when $\sigma_z^\infty = 1$ MPa.

$$F_{\sigma}^{Side}(y)=\frac{K_{\sigma}^{Side}(y)}{\sigma_z^{\infty}W^{1-\lambda}}=\frac{\lim_{r\to 0}\left[r^{1-\lambda}\times\sigma_z^{R}(r,y)\right]}{\sigma_z^{\infty}W^{1-\lambda}} \tag{8}$$

Here, σ_z^{∞} is the z-direction normal stress in the distance. In equation (4), λ is a singularity index, which is obtained by solving the characteristic equation [18,19] of equation (1).

As described above, in this study a mesh-independent technique named proportional method [12] is extended to analyzing the 3D ISSF distributions. Recently, the proportional method was extended to analyzing the vertex ISSF of 3D bonded interface in Fig. 9 [20]. Fig. 9 illustrates the vertex ISSF K_{σ}^{vtx} at $(x, y, z) = (-W/2, -W/2, 0)$ in Fig. 7(a) where the ISSF K_{σ}^{2D} at $(x, y)=(-W/2, 0)$ in Fig. 3 (a) is used as the reference solution. In Fig. 9, the local polar coordinate (r, ϕ) is set at the vertex $(x, y, z) = (-W/2, -W/2, 0)$. The notation ϕ denotes the angle between the interface end $y = -W/2$ and r axis. Koguchi et al. [17] expressed the singular stress field at $(-W/2, -W/2, 0)$ when $\phi = \pi/4$ by the following equation.

$$\sigma_z^{vtx}(r,\phi=\pi/4)=\frac{K_{\sigma}^{vtx}|_{\phi=\pi/4}}{r^{1-\lambda_{vtx}}} \tag{9}$$

3. ISSF variation for 3D butt joints and debonding condition

As shown in Table 2, the FEM stress ratio is independent of the FEM mesh size having 3-digit accuracy in all the range $|x/W| \leq 0.5$ and $|y/W| \leq 0.5$ along the interface outer edge. Table 3 is obtained from the stress ratio $\sigma_z^{F}(0)/\sigma_z^{REF,F}(0)$, which can be regarded as the ISSF ratio $K_{\sigma,h/W=0.01}^{Side}/K_{\sigma,h/W=1}^{Side}$. Fig. 10 shows the ISSF distribution for h/W = 0.01–1 obtained in the same manner as Table 3. The ISSF ratio distributions $K_{\sigma}^{Side}(y)/K_{\sigma,h/W=1}^{Side}(y)$ are constant except around the corner. Near the corner the ISSF starts decreasing with increasing y/W.

Table 3 also shows another ISSF ratio $K_{\sigma}^{Side}(y)/K_{\sigma}^{2D}$ normalized by the 2D plain strain solution when $h/W = 1$, which is corresponding to the 3D joint when the displacement in the y-directions are constrained (see Fig. 7). Because the singular index at the corner point $y = W/2$ is larger than the singular index along the side, the ratio $K_{\sigma}^{Side}(y)/K_{\sigma}^{2D}$ goes to infinity at the corner, but 3-digit accuracy can be seen outside the corner $y < W/2$. When $\sigma_z^{\infty} = \sigma = 1$ MPa and $W = 1$ mm, the critical ISSF $K_{\sigma,h/W=1}^{2D} = 0.413$ MPa· $m^{0.315}$ was obtained as the 2D bonded plate [12]. Using this result, the ISSF variation $K_{\sigma}^{Side}(y)$ can be indicated in Table 3. Since $K_{\sigma,h/W=0.01}^{Side}/K_{\sigma,h/W=1}^{Side}$ and $K_{\sigma,h/W=1}^{2D}$ are finite at $y = W/2$, $K_{\sigma,h/W=0.01}^{Side}$ goes to infinity as $K_{\sigma,h/W=1}^{Side}/K_{\sigma,h/W=1}^{2D}$ goes to infinity. Table 3 shows the ISSF values have 3-digit accuracy and independent of the FEM mesh when $y/W \leqq 0.4994$ since only at the corner point $y = W/2$ the different singular stress field exists.

Fig. 11 shows the ISSF distributions along the interface side under

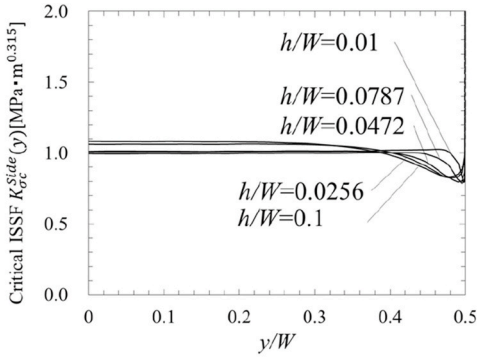

(a) Critical ISSF distribution for combination A in Table 1

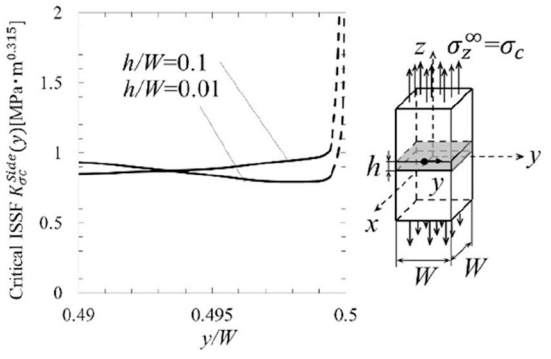

(b) Detail of $y/W = 0.49$~0.50 when h/W=0.1 and 0.01 for combinaion A in Table 1

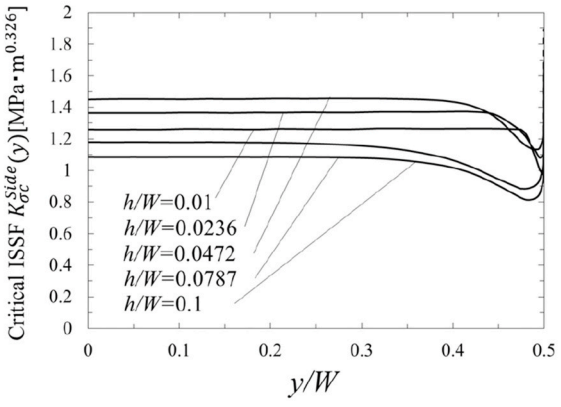

(c) Critical ISSF distribution for combination B in Table 1

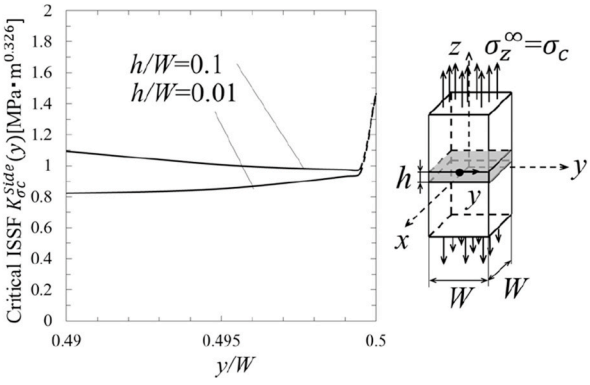

(d) Detail of $y/W = 0.49$~0.50 when h/W=0.1 and 0.01 for combinaion B in Table 1

Fig. 12. Critical ISSF distributions $K_{\sigma c}^{Side}(y)$ when $\sigma_z^{\infty}=\sigma_c$

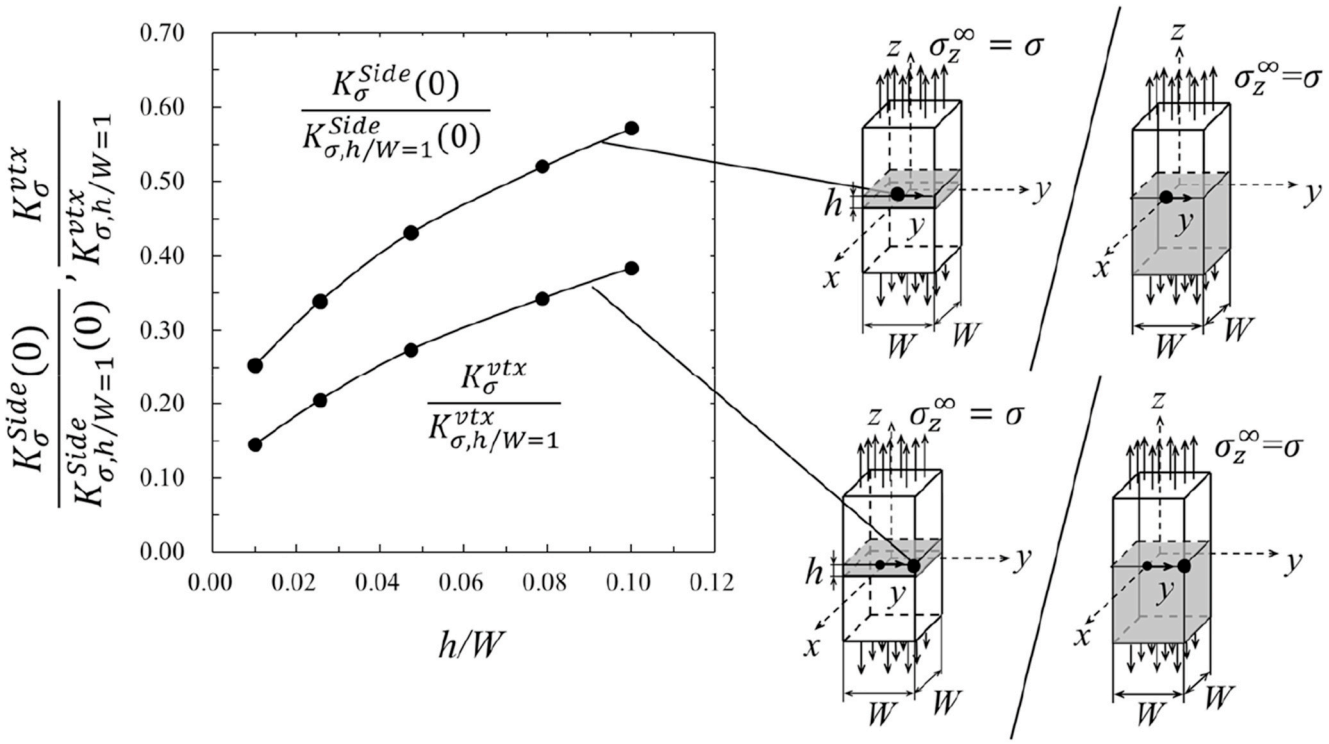

(a) For combination A

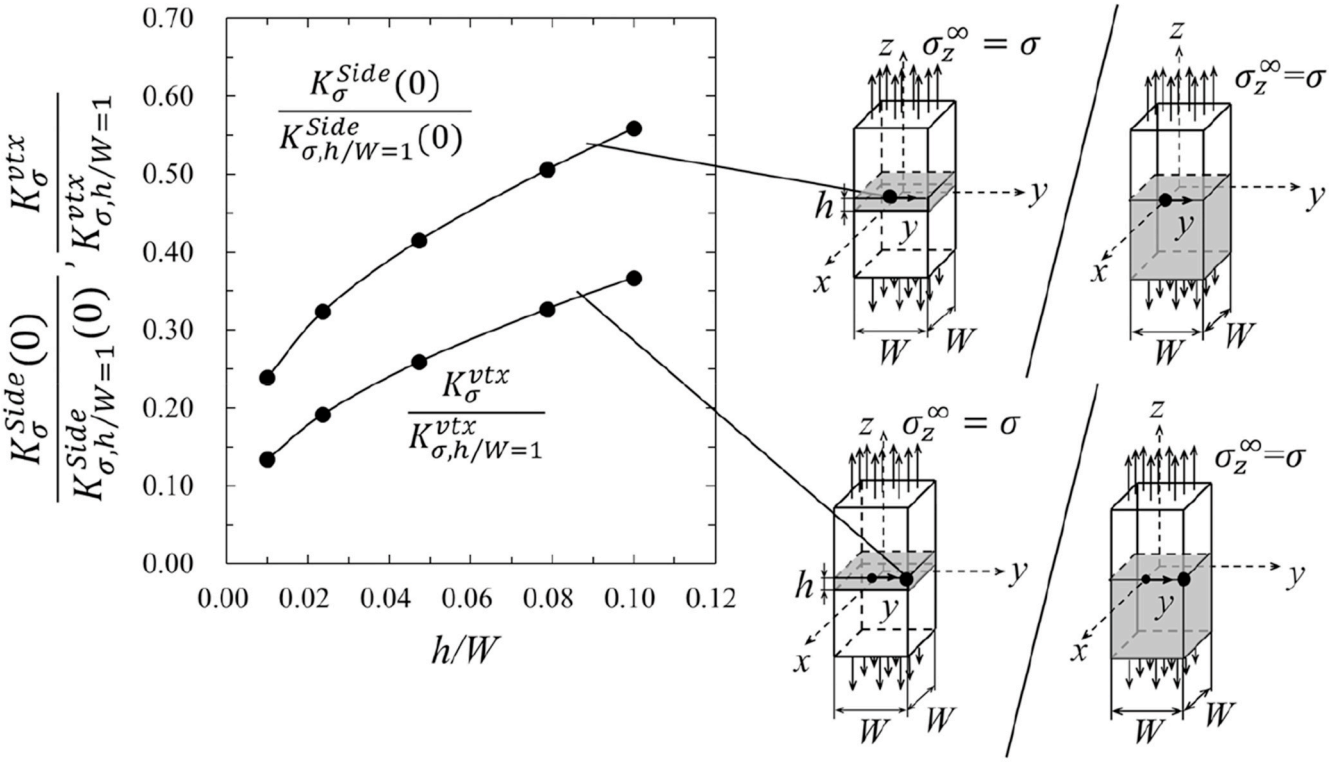

(b) For combination B

Fig. 13. ISSF ratio $K_\sigma^{Side}(y)/K_{\sigma,h/W=1}^{Side}(y)$ focusing on the points at $(x, y) = (W/2,0)$ and $(x, y) = (W/2, W/2)$.

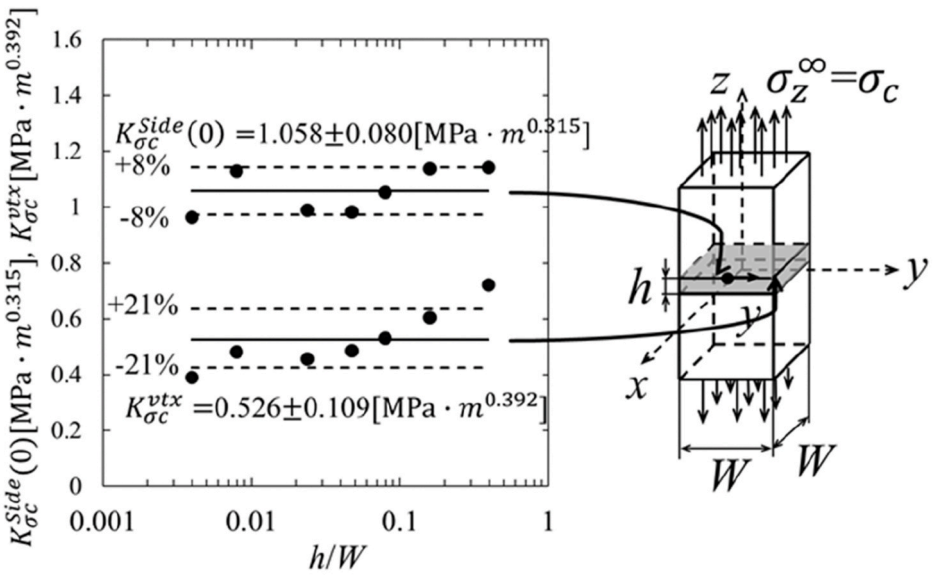

(a) For combination A

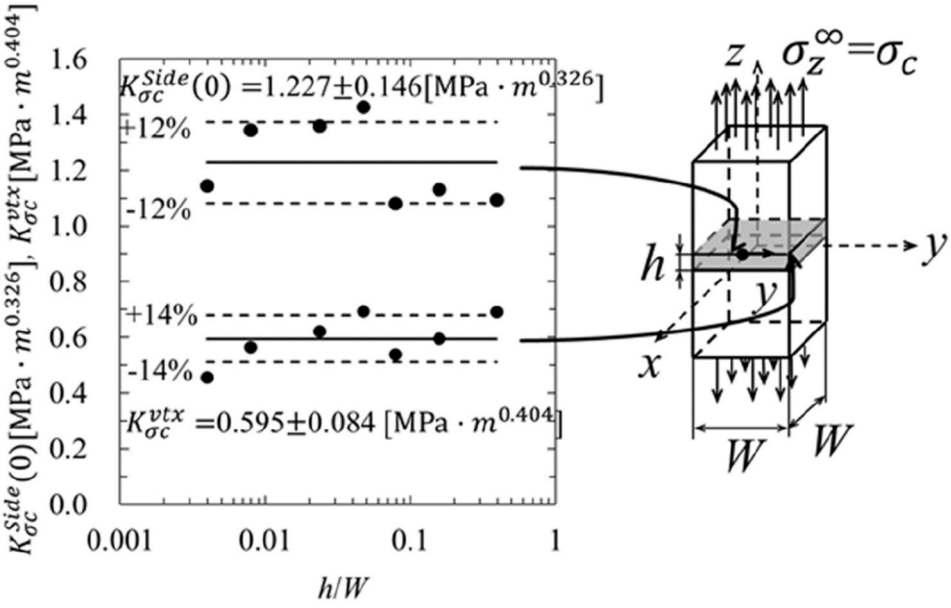

(b) For combination B

Fig. 14. Critical ISSF focusing on the points $(x, y) = (W/2, 0)$ and $(x, y) = (W/2, W/2)$.

remote tensile stress $\sigma_z^{\infty} = 1$. It is seen that ISSF K_{σ}^{Side} decreases with decreasing the adhesive thickness. The details of ISSF near the interface vertex ($0.49 \leq y \leq 0.5$) are shown in Fig. 11 (b), (c). As shown in the range of $0.4995 \leq y \leq 0.5$ in Fig. 11 (b), (c), (e), (f), the ISSFs expressed by the dotted lines go to infinity because different singular stress field exists at the vertex [13,14].

Fig. 12 shows the critical ISSF distributions of $K_{\sigma c}^{Side}$ along the interface side when the debonding occurs at $\sigma_z^{\infty} = \sigma_c$. In Fig. 12, $K_{\sigma c}^{Side}$ is obtained from the adhesive strength $\sigma_c$in Suzuki's experiment [16] and $K_{\sigma}^{Side}(y)$ in Fig. 11 as shown in equation (8).

$$K_{\sigma c}^{Side}(y) = K_{\sigma}^{Side}(y) \quad \text{when } \sigma_z^{\infty} = \sigma_c$$
$$= F_{\sigma}^{Side}(y)\sigma_z^{\infty} W^{1-\lambda}|_{\sigma_z^{\infty} = \sigma_c} \tag{10}$$

Fig. 12 (a) shows $K_{\sigma c}^{Side}(y)$ for resin A is almost constant independent of h/W except around the corner and the constant value almost agrees with the two-dimensional result $K_{\sigma c} = 1.039 \pm 0.0643$ MPa· $m^{0.315}$. Fig. 12 (c) shows $K_{\sigma c}^{Side}(y)$ for resin B has some scatter but in a narrow band region. Both critical ISSF variations can be expressed as a single curve with small scatter including the interface corner independent of

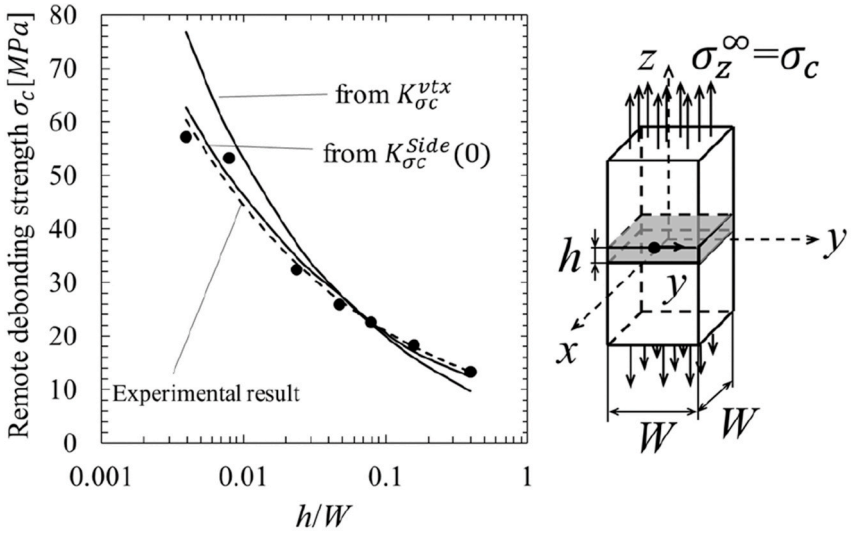

(a) For combination A

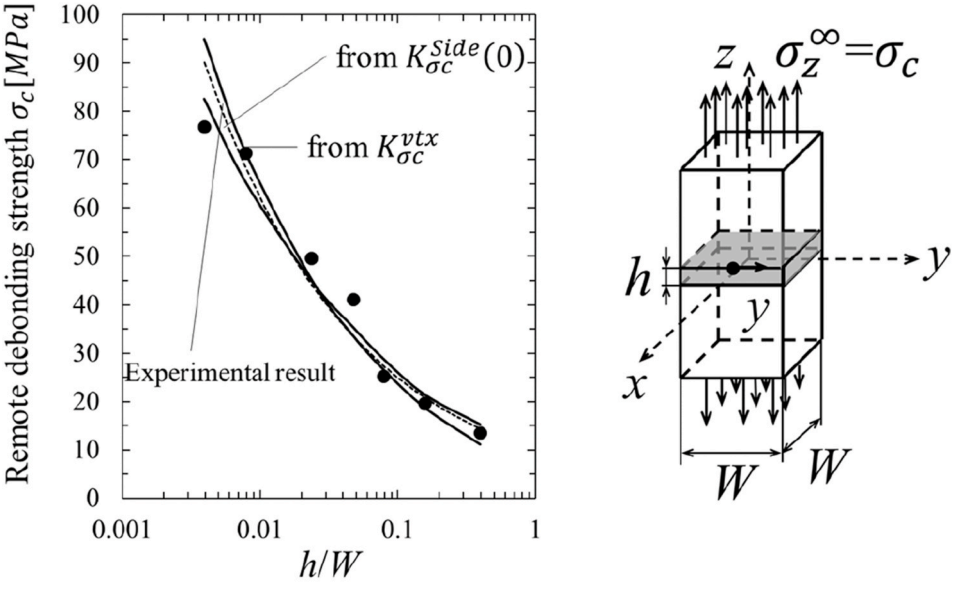

(b) For combination B

Fig. 15. Critical tensile stress σ_c obtained from $K_{\sigma c}^{Side}(0)$ and.$K_{\sigma c}^{Side}(W/2)$

the adhesive thickness. The detail of the scatter is indicated in Table A1 in Appendix A.

Fig. 13 shows the ISSF ratios $K_{\sigma}^{Side}(0)/K_{\sigma,h/W=1}^{Side}(0)$ at the middle interface side and $K_{\sigma}^{vtx}/K_{\sigma,h/W=1}^{vtx}$ at the corner under $\sigma_z^{\infty}=\sigma$. Both ISSFs decrease with decreasing the adhesion layer thickness h/W. In Fig. 13, $K_{\sigma}^{vtx}/K_{\sigma,h/W=1}^{vtx}$ is always smaller than $K_{\sigma}^{Side}(0)/K_{\sigma,h/W=1}^{Side}(0)$. The ISSF ratio $K_{\sigma}^{Side}(y)/K_{\sigma,h/W=1}^{Side}(y)$ becomes smaller due to the larger interaction between the two adhesive interfaces. In other words, the interaction effect is significant at the interface corner $y=W/2$.

Fig. 14 shows the critical ISSFs $K_{\sigma c}^{vtx}$ and $K_{\sigma c}^{Side}(0)$ when the debonding occurs. As shown in Fig. 14, those values $K_{\sigma c}^{Side}(0)$ and $K_{\sigma c}^{vtx}$ are constant regardless of h. In Fig. 14, for material combination A, the constant value of $K_{\sigma c}^{Side}(0)=1.058\pm0.080[MPa{\cdot}m^{0.315}]$ is almost the same as $K_{\sigma c}^{2D}=1.039\pm0.0643[MPa{\cdot}m^{0.315}]$ in Fig. 1 obtained by 2D analysis; and for material combination B, the constant value of $K_{\sigma c}^{Side}(0)=1.227\pm0.146$ $[MPa{\cdot}m^{0.326}]$ is almost the same as $K_{\sigma c}^{2D}=1.203\pm0.144[MPa{\cdot}m^{0.326}]$.

Fig. 15 shows the critical tensile stress σ_c (solid line) can be obtained from the average values of $K_{\sigma c}^{Side}(0)$ and $K_{\sigma c}^{vtx}$ in Fig. 14 in comparison with the experimentally obtained σ_c (dotted line). In Fig. 15, both results of σ_c from $K_{\sigma c}^{Side}(0)$ and $K_{\sigma c}^{vtx}$ in Fig. 13 are in good agreement with the experiment. In other words, the debonding strength σ_c can be predicted from both $K_{\sigma c}^{Side}(0)$ and $K_{\sigma c}^{vtx}$ in Fig. 14. This is because the critical ISSF variations are quite similar independent of the adhesive thickness h as shown in Fig. 12 (a). Since the 2D ISSF analysis may provide the same results of $K_{\sigma c}^{Side}(0)$, simple 2D analysis can be used conveniently to predict the adhesive strength. The present study shows that the adhesion strength can be evaluated with sufficient accuracy by the analysis of the two-dimensional model without using complicated 3D analysis including different singular stress field at interface corners.

As shown in Figs. 14 and 15, for Carbon Steel/Epoxy resin, the specimen reaches a critical condition at the side at exactly the same load as the specimen reaches the critical condition at the corner. Similar conclusions can be expected for Aluminum/Araldite and Blass/Solder since the debonding condition can be expressed in a similar way as ISSF = const [14]. Care should be taken for applying the ISSF method to ductile adhesives such as a rubber-modified epoxy whose fracture toughness varies depending on the crack length [21].

4. Conclusion

In this study, the ISSF variation was analyzed along the interface outer edge of the 3D prismatic butt joint since previously 2D modelling was used without validity confirmation. The obtained 3D ISSF was used to explain the debonding condition of the experimental results of the prismatic butt joint. The conclusions obtained are summarized as follows.

(1) The ISSF variation was analyzed very accurately. Mesh independent proportional method was presented to analyze 3D geometries since previously only 2D problems were treated. The FEM stress ratio was focused along the interface outer edge to analyze different adhesive layer thicknesses.
(2) The obtained ISSF variations are almost constant about in the 90% middle range of the interface side except near the corner. The critical ISSF variation at the time of debonding is expressed as a single curve with small scatter including the interface corner independent of the adhesive thickness.
(3) The adhesive strength can be expressed as a constant value of the ISSF at the center side and also at the corner of the adhesive interface.Debonding stress can be predicted from the critical ISSFs because the experimental values can be obtained from both the center and the corner of the adhesive interface. Since the center ISSF is equal to the ISSF under plane strain, the adhesive strength can be predicted with sufficient accuracy by analyzing the simple two-dimensional model without using a complicated 3D FEM analysis.

As shown in conclusion (3), for Carbon Steel/Epoxy resin, the specimen reaches a critical condition at the side at exactly the same load as the specimen reaches the critical condition at the corner. Similar conclusions can be expected for Aluminum/Araldite and Blass/Solder since the debonding condition can be expressed in a similar way as ISSF = const [14]. Care should be taken for applying the ISSF method to extremely ductile adhesives such as a rubber-modified epoxy whose fracture toughness varies depending on the crack length [21].

Appendix A. Accuracy of the ISSF method to predict the adhesive strength

Table A1 shows the adhesive strength details obtained experimentally and analytically to clarify the ISSF prediction accuracy. As shown in Table A1(a), the original experimental data include about 10% scatter under the fixed adhesive thickness h. Table A1(b) and Table A1(c) shows that the ISSF $K_{\sigma c}^{2D}$ and $K_{\sigma c}^{Side}$ may predict the adhesive strength within 7% error for S35C/Epoxy resin A and within 12% error for S35C/Epoxy resin B independent of adhesive thickness h. On the other hand, Table A1 (d) shows that the ISSF at the vertex $K_{\sigma c}^{vtx}$ in Table A1 (d) may predict the adhesive strength within 21% error for S35C/Epoxy resin A and 13% error for S35C/Epoxy resin B independent of adhesive thickness h. This scatter is a bit larger than the scatters of $K_{\sigma c}^{2D}$ and $K_{\sigma c}^{Side}$.

The ISSF prediction accuracy can be discussed in relation to the original experimental data by taking 2D modelling. In Fig. 1, the 2D ISSF may predict the average adhesive strength within 7% error for S35C/Epoxy resin A, and within 12% error for S35C/Epoxy resin B. Similarly, in Ref. [14], the 2D ISSF may predict the average adhesive strength within 5% error for Aluminum/Araldite and within 16% error for Blass/Solder. It should be noted that such errors are caused by the experimental results. As shown in Table A1, for resin A the average values were obtained from 5 specimens and for resin B only from 3 specimens. Fig. 2 illustrates that the obtained average strength sometimes smaller and sometimes larger than the fitted curve.

Considering the experimental scatter, the ISSF method may predict all experimental data with 25% error at most. This maximum error consists of the average value's error and the experimental scatter. If the average value can be obtained more accurately, for example, by increasing the number of the specimens, the ISSF prediction accuracy may coincide with the scatter of the original experimental results. In other words, the accuracy of the ISSF method can be improved if the average values can be obtained more accurately.

Table A1
Experimentally and analytically obtained adhesive strength

(a) Adhesive strength expressed by for remote tensile stress

		(i) S35C/Epoxy resin A						(ii) S35C/Epoxy resin B			
		Strength						Strength			
h	h/W	Debonding strength σ_c[MPa]					Average ± SD[MPa]	Debonding strength σ_c[MPa]			Average ± SD[MPa]
0.05	0.00394	47.7	50.0	58.4	63.5	66.5	57.2 ± 7.34	72.8	77.6	79.9	76.8 ± 2.96
0.10	0.00787	44.3	49.8	52.0	57.0	63.5	53.3 ± 6.52	70.2	71.5	72.6	71.4 ± 0.98
0.30	0.0236	28.6	30.8	32.5	34.2	36.5	32.5 ± 2.72	45.5	50.9	52.6	49.7 ± 3.03
0.60	0.0472	21.9	24.8	25.2	28.2	29.6	25.9 ± 2.71	39.6	40.0	43.9	41.2 ± 1.94
1.00	0.0787	21.5	21.5	21.9	23.5	24.4	22.6 ± 1.18	21.1	26.5	28.4	25.3 ± 3.09
2.00	0.157	14.8	18.1	18.2	19.9	20.9	18.4 ± 2.08	18.1	19.7	21.3	19.7 ± 1.31
5.00	0.394	11.4	11.4	13.6	15.0	15.6	13.4 ± 1.76	12.4	12.4	16.0	13.6 ± 1.70

SD: Standard deviation.

(b) Adhesive strength expressed by ISSF obtained by 2D modelling

	(i) S35C/Epoxy resin A			(ii) S35C/Epoxy resin B		
h/W	σ_c[MPa]	F_σ^{2D}	$K_{\sigma c}^{2D}$[MPa.m$^{0.315}$] Average ± SD	σ_c[MPa]	F_σ^{2D}	$K_{\sigma c}^{2D}$[MPa.m$^{0.326}$] Average ± SD
0.00394	57.2	0.0671	0.970 ± 0.125	76.8	0.0620	1.147 ± 0.044
0.00787	53.3	0.0831	1.120 ± 0.137	71.4	0.0778	1.339 ± 0.018
0.0236	32.5	0.119	0.978 ± 0.082	49.7	0.112	1.342 ± 0.082
0.0472	25.9	0.150	0.981 ± 0.102	41.2	0.142	1.411 ± 0.066
0.0787	22.6	0.178	1.017 ± 0.053	25.3	0.171	1.042 ± 0.127
0.157	18.4	0.231	1.071 ± 0.121	19.7	0.223	1.060 ± 0.070
0.394	13.4	0.335	1.135 ± 0.149	13.6	0.331	1.085 ± 0.135
$K_{\sigma c(average)}$			1.039 ± 0.064			1.204 ± 0.144

(c) Adhesive strength expressed by ISSF obtained by 3D modelling at the interface side

	(i) S35C/Epoxy resin A			(ii) S35C/Epoxy resin B		
h/W	σ_c[MPa]	F_σ^{Side}	$K_{\sigma c}^{Side}$[MPa.m$^{0.315}$] Average ± SD	σ_c[MPa]	F_σ^{Side}	$K_{\sigma c}^{Side}$[MPa.m$^{0.326}$] Average ± SD
0.00394	57.2	0.0669	0.966 ± 0.139	76.8	0.0619	1.144 ± 0.054
0.00787	53.3	0.0840	1.130 ± 0.155	71.4	0.0783	1.346 ± 0.023
0.0236	32.5	0.120	0.989 ± 0.093	49.7	0.114	1.361 ± 0.102
0.0472	25.9	0.151	0.983 ± 0.115	41.2	0.144	1.428 ± 0.082
0.0787	22.6	0.185	1.055 ± 0.062	25.3	0.178	1.082 ± 0.162
0.157	18.4	0.245	1.138 ± 0.144	19.7	0.239	1.132 ± 0.092
0.394	13.4	0.338	1.144 ± 0.168	13.6	0.334	1.094 ± 0.167
$K_{\sigma c(average)}$			1.058 ± 0.080			1.227 ± 0.146

(d) Adhesive strength expressed by ISSF obtained by 3D modelling at the interface corner

	(i) S35C/Epoxy resin A			(ii) S35C/Epoxy resin B		
h/W	σ_c[MPa]	F_σ^{vtx}	$K_{\sigma c}^{vtx}$[MPa.m$^{0.392}$] Average ± SD	σ_c[MPa]	F_σ^{vtx}	$K_{\sigma c}^{vtx}$[MPa.m$^{0.404}$] Average ± SD
0.00394	57.2	0.0380	0.392 ± 0.056	76.8	0.0347	0.457 ± 0.022
0.00787	53.3	0.0502	0.482 ± 0.066	71.4	0.0462	0.565 ± 0.010
0.0236	32.5	0.0782	0.458 ± 0.043	49.7	0.0729	0.621 ± 0.046
0.0472	25.9	0.104	0.487 ± 0.057	41.2	0.0982	0.694 ± 0.040
0.0787	22.6	0.131	0.532 ± 0.031	25.3	0.124	0.539 ± 0.081
0.157	18.4	0.183	0.606 ± 0.077	19.7	0.177	0.596 ± 0.048
0.394	13.4	0.300	0.724 ± 0.106	13.6	0.297	0.691 ± 0.106
$K_{\sigma c(average)}$			0.526 ± 0.109			0.595 ± 0.078

Appendix B. Step-by-step procedure to apply the proportional method to calculate ISSF in any 3D bonded geometries

Fig. B1 illustrates how to calculate the ISSF in any 3D bonded geometries by applying the proportional method. As shown in the conclusions (2) and (3), 2D modelling is sometimes useful although the validity confirmation is desirable. The flowchart in Fig. B1 indicates elementary step-by-step actions. Here, a cylindrical butt joint in Fig. B2 [22] is assumed as an example.

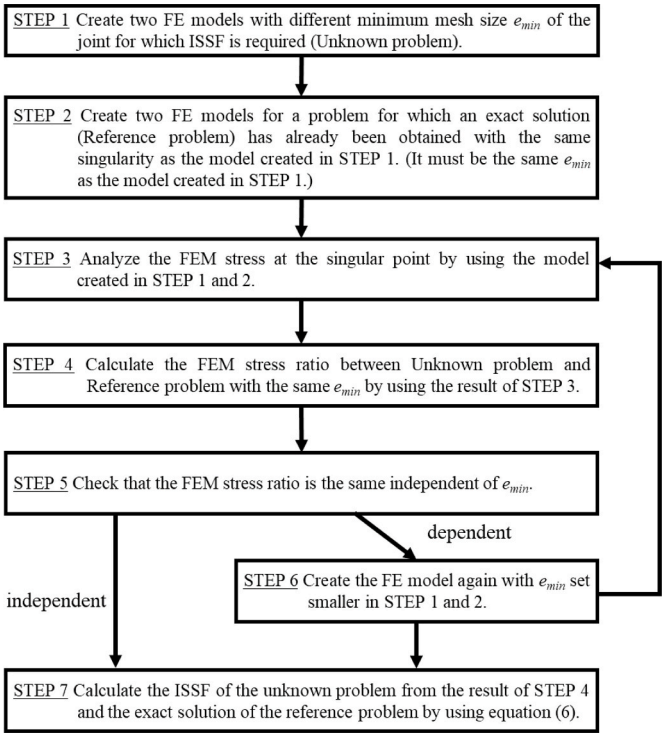

Fig. B1. Flowchart for applying the proportional method to any geometries

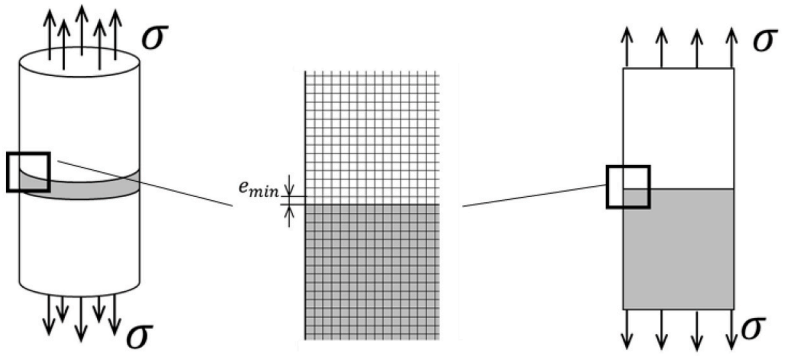

(a) Cylindrical butt joint (Unknown problem) [22]

(b) 2D bonded plate (Reference problem)

Fig. B2. Example of analysis model and mesh pattern

First of all, as STEP 1, two kinds of minimum FE mesh size e_{min} are applied to the cylindrical butt joint (=unknown problem). Next, as STEP 2, those two kinds of minimum FE mesh size e_{min} are applied to the bonded plate (=reference problem) whose exact solution is available [12]. Note that the reference problem and the unknown problem have the same singular stress field but different ISSF. As STEP 3, the FEM stresses at the singular points are calculated for the unknown and the reference problems by applying FEM. As STEP 4, the FEM stress ratio of the unknown and reference problems is obtained. This is because the FEM stress around the singular point is not the real stress and depends on the FEM mesh size. As STEP 5, the mesh-independency of the stress ratio is investigated. Since the same FEM mesh is applied around the singular point, the FEM error can be eliminated. STEP 6 is required when two ratios are not the same. Instead, if two ratios are the same, as STEP 7, the FEM stress ratio can be used as the ISSF ratio. Then, the ISSF of the unknown problem can be provided from the ISSF ratio and the exact ISSF of the reference problem. In the case of STEP 6, since the previous mesh sizes are not appropriate, the new FE models are newly created using smaller mesh size and go to STEP3.

References

[1] Barnes TA, Pashby IR. Joining techniques for aluminum spaceframes used in automobiles: part II – adhesive bonding and mechanical fasteners. J Mater Process Technol 2000;99:72–9.

[2] Higgins A. Adhesive bonding of aircraft structures. Int J Adhesion Adhes 2000;20 (5):367–76.

[3] Petrie EM. Adhesives for the assembly of aircraft structures and components: decades of performance improvement, with the new applications of the horizon. Met Finish 2008;106(2):26–31.

[4] Lörinci G, Matuschek G, Fekete J, Gebefügi I, Kettrup A. Investigation of thermal degradation of some adhesives used in the automobile industry by thermal analysis/mass spectrometry and GC–MS. Thermochim Acta 1995;263:73–86.

[5] Barnes TA, Pashby IR. Joining techniques for aluminium spaceframes used in automobiles: part II — adhesive bonding and mechanical fasteners. J Mater Process Technol 2000;99(1–3):72–9.

[6] Xuemei W, Vijay G. Construction and characterization of chemically joined stainless steel/E-glass composite sections. Mech Mater 2005;37(12):1198–209.

[7] Jarry E, Shenoi RA. Performance of butt strap joints for marine applications. Int J Adhesion Adhes 2006;26(3):162–76.

[8] Encinas N, Oakley BR, Belcher MA, Blohowiak KY, Dillingham RG, Abenojar J, Martínez MA. Surface modification of aircraft used composites for adhesive bonding. Int J Adhesion Adhes 2014;50:157–63.

[9] Qian Z, Akisanya AR. An experimental investigation of failure initiation in bonded joints. Acta Mater 1998;46(14):4895–904.

[10] Akisanya AR, Meng CS. Initiation of fracture at the interface corner of bi-material joints. J Mech Phys Solid 2003;51:27–46.

[11] Mintzas A, Nowell D. Validation of an Hcr -based fracture initiation criterion for adhesively bonded joints. Eng Fract Mech 2012;80:13–27.

[12] Zhang Y, Noda NA, Wu P, Duan ML. A mesh-independent technique to evaluate stress singularities in adhesive joints. Int J Adhes Adhes 2015; 57: 105–17; Corrigendum of authorship "A mesh-independent technique to evaluate stress singularities in adhesive joints". Int J Adhesion Adhes 2015;60:130.

[13] Li R, Noda NA, Takaki R, Sano Y, Takase Y, Miyazaki T. Most suitable evaluation method for adhesive strength to minimize bend effect in lap joints in terms of the intensity of singular stress field. Int J Adhesion Adhes 2018;86:45–58.

[14] Noda NA, Miyazaki T, Li R, Uchikoba T, Sano Y, Takase Y. Debonding strength evaluation in terms of the intensity of singular stress at the corner with and without fictitious crack. Int J Adhesion Adhes 2015;61:46–64.

[15] Yuki R, Ishikawa H, Kishimoto K, Xu JQ. Mechanics of interface. Baifukan; 1993 [in Japanese].

[16] Suzuki Y. Adhesive tensile strengths of scarf and butt joints of steel plates (relation between adhesive layer thicknesses and adhesive strengths of joints). Jpn Soc Mech Eng Int J 1987;30(265):1042–51.

[17] Koguchi H, Muramoto T. The order of stress singularity near the vertex in three-dimensional joints. Int J Solid Struct 2000;66(648):1597–605.

[18] Bogy DB. Edge- bonded dissimilar orthogonal elastic wedges under normal and shear loading. Trans ASME, J Appl Mech 1968;35:460–6.

[19] Bogy DB. Two edge-bonded elastic wedges of different materials and wedge angles under surface tractions, trans ASME. J Appl Mech 1971;38:377–86.

[20] Miyazaki T, Inoue T, Noda NA. Practical method for analyzing singular index and intensity of singular stress field for three dimensional bonded plate. IOP Conf Ser Mater Sci Eng 2018;372(1):012002.

[21] Kin Loch AJ, Shaw SJ. The fracture resistance of a toughened epoxy adhesive. J Adhes 1981;12:59–77.

[22] Noda NA, Ren F, Takaki R, Wang Z, Oda K, Miyazaki T. Intensity of singular stress field over the entire bond line thickness range useful for evaluating the adhesive strength for plate and cylinder butt joints. Int J Adhesion Adhes 2018;85:234–50.